

ESTIMATING RADIATED EMISSION REDUCTION FROM PRINTED CIRCUIT BOARD USING VECTOR NETWORK ANALYZER WITH A BULK CURRENT INJECTION PROBE

Cheng-Yu Ho^{*}, Kai-Syuan Chen, and Tzyy-Sheng Horng

Department of Electrical Engineering National Sun Yat-Sen University
No. 70, Lien-Hai Road, Kaohsiung 804, Taiwan

Abstract—A vector network analyzer (VNA) with a bulk current injection (BCI) probe is proposed to measure the transmission coefficient of a PCB. The purpose of developing such a measurement techniques is to predict the radiated emission for good correlation with the fully-anechoic chamber measured results. In this study, the proposed method is used to determine the radiated emission from a DC supply loop. Moreover, the proposed method can be further used to accurately predict the reduction of radiated emission from the improved DC supply loop. Electromagnetic simulations is also developed to confirm the accuracy of the proposed techniques.

1. INTRODUCTION

Radiated emission from printed circuit boards (PCBs) is very complex and difficult to resolve. The main problem is the lack of reliable and convenient methods for analyzing and predicting PCB radiation. Until now, therefore, methods of diagnosing and solving problems of PCB radiated emission rely mostly on empirical experiences [1–3]. The difficulty in methods of predicting PCB radiated emission by simulation is the combination of circuit and electromagnetic models of practical interactions between integrated circuits and PCB traces [4]. Far-field radiated emission can be measured in a fully-anechoic chamber to obtain the spectrum that is used to evaluate conformity to electromagnetic compatibility (EMC) regulations [5–8]. However, performing far-field measurements is very costly and time-consuming. Another common method of measuring PCB

Received 1 November 2012, Accepted 5 December 2012, Scheduled 10 December 2012

* Corresponding author: Cheng-Yu Ho (d943010018@student.nsysu.edu.tw).

radiated emissions is to use a magnetic or electric field probe for the near-field scanning of the PCB surface [9–13]. Although the associated test setup and procedure are simpler than those for far-field measurement, the near-field scan results are more helpful in locating the source of radiated emission than for predicting radiated emission levels as required in EMC specifications. In recent years, the vector network analyzer (VNA) measurement has shown potential in EMC applications because it can be used to measure S -parameters, which correlate with the electromagnetic emission and susceptibility. Applications of VNA include measuring the S -parameters that describe the conversion from differential to common mode to elucidate the radiation mechanisms [14, 15], and measuring the transfer function of the coupling path which is correlated with conducted susceptibility [16]. By coupling external disturbance to harness, bulk current injection (BCI) probes have also proven effective for simulating radiation-induced effects in conducted susceptibility tests [17].

The authors' previous work [18] presented a method of measuring the transmission coefficient by using a VNA and a BCI probe to characterize the common-mode radiation from a DC supply loop of a thin film transistor-liquid crystal display (TFT-LCD) panel. By expanding the measurement method of [18], this paper provides a detailed calibration procedure to determine the frequency-dependent transfer impedance of BCI probe. The probe equivalent circuit model developed allows precise prediction of the BCI probe behavior for frequencies up to 400 MHz. As a practical application, the proposed method can be employed to determine the radiated emission from PCB and to predict the improved radiated emission obtained by selecting a reasonable value of the decoupling capacitor on a PCB.

2. CALIBRATION PROCEDURE OF MEASUREMENT PROBE

2.1. Transfer Impedance of Measurement Probes

In this work, a BCI probe was used to measure common-mode current on a PCB. To measure accurately the common-mode current on a PCB, the BCI probe must be calibrated to determine the transfer impedance [17]. The BCI probe F-130-1A is designed for frequencies up to 400 MHz. Figure 1(a) shows the experimental setup for measuring the transfer impedance of a BCI probe. The default process of calibration is performed using a calibration fixture, in which the BCI probe is mounted. The transfer impedance of a BCI probe is measured under a specified load of $50\ \Omega$. As shown in Figure 1(a), port 1 of the

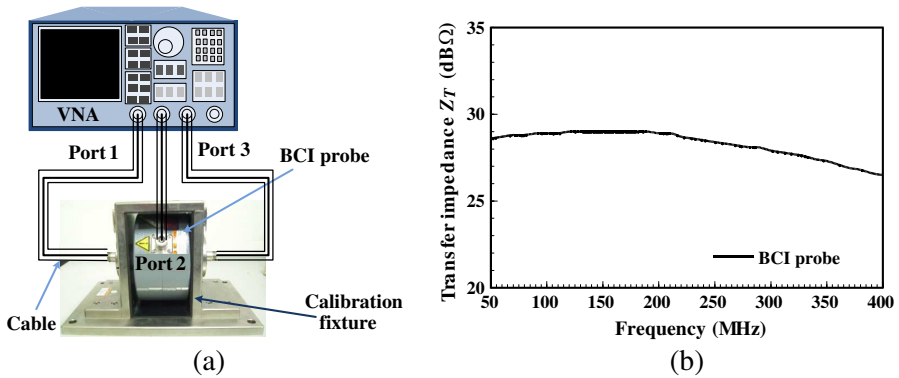


Figure 1. Experimental setup for measuring transfer impedance of BCI probe using calibration fixture. (a) Corresponding photograph. (b) Measurement result of transfer impedance.

VNA is connected to the input port of the calibration fixture, port 2 is connected to the BCI probe and port 3 is connected to the output port of the calibration fixture. The excitation of the input port generates currents in the cable of the calibration fixture and induces a voltage on the BCI probe. By definition, the transfer impedance relates the current in the cable of the calibration fixture to the voltage at the BCI probe output. The transfer impedance of the BCI probe is given by

$$Z_T(\omega) = \frac{V_2}{I_1} = 50 \cdot S_{21,fixture}(\omega). \quad (1)$$

In this formula, V_2 is the output voltage of BCI probe loaded with 50Ω in most case and I_1 the current flowing in the coaxial line of calibration fixture. The S_{21} measurement ($S_{21,fixture}$) is the transmission scattering parameter measured by the VNA. The magnitude transfer impedance $Z_T(\omega)$ is obtained in dBΩ from the S -parameter $S_{21,fixture}(\omega)$, which can be measured in the calibration procedure. As shown in Figure 1(b), the BCI probe has a frequency-dependent transfer impedance ranging from 26 to 28 dBΩ in the frequency range of 50–400 MHz.

2.2. Modeling of Measurement Probes

The modeling and EM simulation of the BCI probe are now described. Figure 2(a) presents the geometrical configuration of the BCI probe and Figure 2(b) depicts the equivalent circuit model of the BCI probe. The BCI probe is consisting of a metallic frame, a toroidal ferrite core, an inner winding and input connector. In the equivalent circuit model of the BCI probe, the toroidal ferrite core has a complex

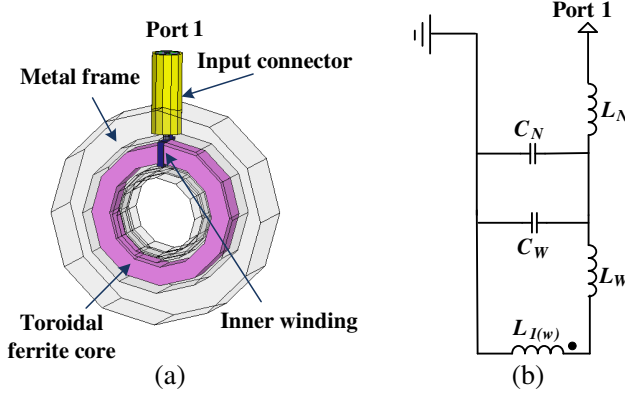


Figure 2. (a) Geometrical configuration. (b) Equivalent circuit model of the BCI probe. ($L_N \approx 3$ nH, $C_N \approx 4$ pF, $L_W = 70$ nH, $C_W = 4$ pF).

permeability characteristic [17]. To obtain the frequency-dependent and lossy characteristics of the toroidal ferrite core of the BCI probe, the reflection coefficient that is measured using the VNA is converted into the input impedance of the BCI probe. The input impedance $Z_{in}(\omega)$ of the BCI probe was measured in the absence of the calibration fixture [17]. The total input impedance of BCI probe is given by

$$Z_{in}(\omega) = j\omega L_N + \left[j\omega (C_N + C_W) + \frac{1}{j\omega [L_W + L_1(\omega)]} \right]^{-1} \quad (2)$$

In this equation for input impedance, parameters L_N and C_N model the effects of the input connector and the adapter. These parameters were estimated from the physical size of the BCI probe. Thus, these parameters are calculated using

$$L_N = \frac{\mu_0}{2\pi} \ln \left(\frac{r_o}{r_i} \right) \quad (H/m) \quad (3)$$

$$C_N = \frac{2\pi\epsilon_0}{\ln \left(\frac{r_o}{r_i} \right)} \quad (F/m) \quad (4)$$

where r_i is the inner radius of the input connector, r_o the outer radius of the input connector, μ_0 the free-space permeability, and ϵ_0 the free-space permittivity.

Parameters L_W and C_W denote the total capacitance and inductance, respectively, between the inner winding and the metallic frame. These parameters can be evaluated by considering in the case of a single wire above a ground plane by treating the metallic frame as

the ground plane. Thus, these parameters can be found as

$$L_W = \frac{\mu_0}{2\pi} \ln \left(\frac{2h}{r_i} \right) \quad (H/m) \quad (5)$$

$$C_W = \frac{2\pi\epsilon_0}{\ln \left(\frac{2h}{r_i} \right)} \quad (F/m) \quad (6)$$

where r_i is the radius of the inner winding and h the height between the inner winding and the metallic frame.

Parameter $L_1(\omega)$ represents the complex and frequency-dependent self inductance of the primary winding of the probe and self-inductance $L_1(\omega)$ in (2), which is given by

$$L_1(\omega) = L_0 [\mu_1(\omega) - j\mu_2(\omega)] \quad (7)$$

where $\mu_1(\omega)$ relates to the magnetic energy stored in the core, and $\mu_2(\omega)$ relates to the losses in the core. L_0 denotes the self-inductance of ferrite core with unity permeability and an unchanged magnetic flux distribution. This parameter depends on the shape and the dimensions of the core of the BCI probe. Hence, the inductance L_0 is estimated as

$$L_0 = \mu_0 \frac{N_1^2 b}{2\pi} \ln \left[\frac{r_c^{(o)}}{r_c^{(i)}} \right] \quad (H/m) \quad (8)$$

where N_1 is the number of turns of the primary winding, μ_0 the free-space permeability, and b , $r_c^{(o)}$ and $r_c^{(i)}$ denote the thickness, the external radius, and internal radius of the toroidal core, respectively.

Figures 3(a) and 3(b) present the magnitude and phase of the return loss of the BCI probe, respectively. The EM simulation and equivalent circuit model agree closely with the measured results over the frequency range 50–400 MHz.

3. COMMON-MODE CURRENT AND RADIATION

3.1. Radiated Emission from TFT-LCD Panel

In this work, the VNA with a BCI probe is applied to determine the radiated emission from a DC supply loop. Empirically, the main contributor to radiated emission is the PCB driver board of TFT-LCD panel [19]. The PCB driver board consists mainly of a timing controller (T-CON), a source driver IC and a DC-to-DC converter. The DC supply loop delivers DC power from the DC-to-DC converter to the source driver IC on the PCB driver board. Notably, a decoupling capacitor in the loop prevents the coupling of high-order harmonics of

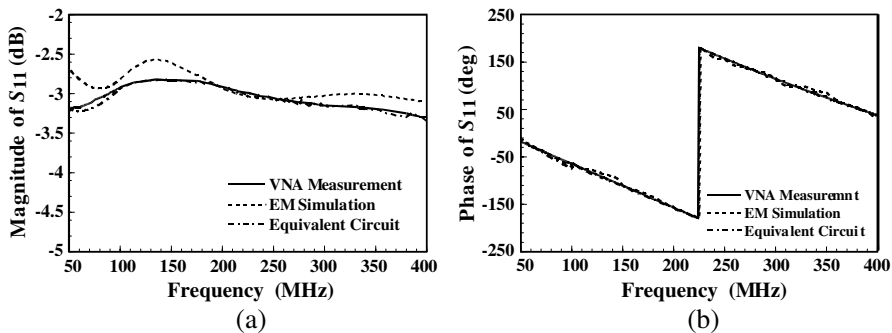


Figure 3. Comparison of S_{11} among VNA measurement, EM simulation and equivalent circuit model of the BCI probe. (a) Magnitude of S_{11} . (b) Phase of S_{11} .

the T-CON to the loop. The T-CON generates a clock signal with short transition time. The clock signal from the T-CON produces radiation and couples to the DC supply loop in the PCB driver board. Experimental experience indicates that EMI source and self-resonance of the coupling path at the same frequency cause significant radiated emission at that frequency. In the radiation mechanism of the TFT-LCD panel, the T-CON may be a major EMI source and the DC supply loop may be a major coupling path.

3.2. Resonance of DC Supply Loop

Radiated emission from PCB happens in very diverse ways [20–22]. The DC supply loop is one of the main radiation mechanisms because it may behave like an antenna, radiating the noise source that is coupled from the T-CON. Empirically, the radiation from a DC supply loop is maximal when resonance occurs. This study therefore characterized the effect of resonance by using a VNA to measure the input impedance of the DC supply loop to power the source driver IC. As shown in Figure 4(a), the DC supply loop is duplicated on another PCB with an area of 20 mm \times 10 mm and then connected to a VNA via a SMA connector. Figure 4(b) displays the equivalent circuit model of the DC supply loop. Parameters C_{dec} , L_e , and R_e are used to model the decoupling capacitor. A SMT decoupling capacitor of 100 nF, an ESL of 0.479 nH, and an ESR of 0.063 Ω , was used to prevent the coupling of high-order harmonics in the driver PCB of TFT-LCD panel. The corresponding element values are $C_{dec} = 100$ nF, $L_e = 0.479$ nH, and $R_e = 0.063$ Ω . Parameter C_{stray} represents the output capacitance of

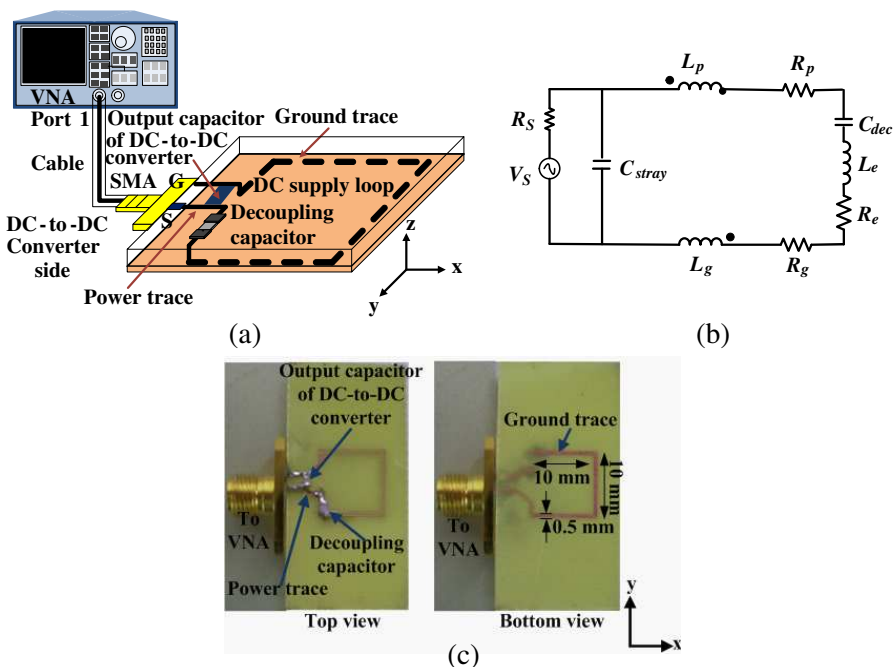


Figure 4. An on-PCB DC supply loop connected to a VNA for measuring its input impedance. (a) Measurement setup. (b) Equivalent circuit model. (c) Photograph and physical dimensions of the DC supply loop.

DC-to-DC converter, and this parameter is estimated using resonator frequency of DC supply loop. The corresponding element values is $C_{stray} = 48\text{ pF}$. Parameters L_p and L_g denote the inductance of the power and ground trace of DC supply loop on PCB and the element values were derived by using Ansys-Ansoft Q3D Extractor. The corresponding element values are $L_p = 4\text{ nH}$, and $L_g = 23\text{ nH}$. Parameters R_p and R_g denote the resistance of the power and ground trace of DC supply loop on PCB and the element values were derived by using Ansys-Ansoft Q3D Extractor. The corresponding element values are $R_p = 0.01\ \Omega$ and $R_g = 0.07\ \Omega$. Figure 4(c) is a photograph showing the physical dimensions of the duplicated DC supply loop.

Figures 5(a) and 5(b) plot the real and imaginary parts, respectively, of the input impedance at frequencies of up to 400 MHz. The measured results clearly demonstrate that the DC supply loop on PCB resonates at 140 MHz. With the PCB trace parasitic elements that are extracted by Ansys Q3D and the equivalent model of the 100-

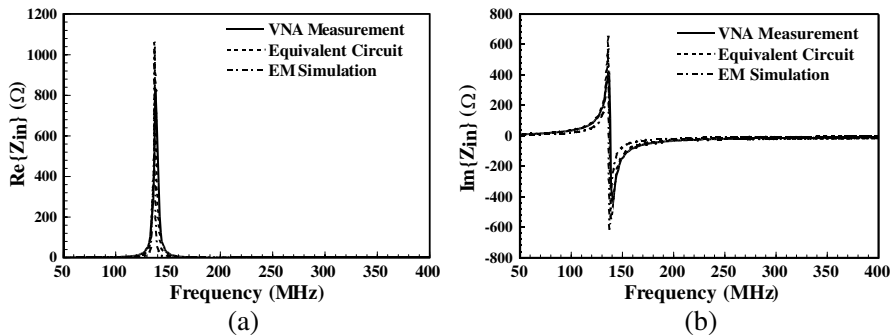


Figure 5. Comparison of input impedance of the DC supply loop among VNA measurement, EM simulation and equivalent circuit model. (a) Input resistances. (b) Input reactances.

nF decoupling capacitor, the equivalent circuit shown in Figure 4(b) can confirm the measured input impedance response of the DC supply loop.

3.3. Common-mode Current on DC Supply Loop

Experimental experience indicates that the noise source is at the same frequency as the self-resonance of the DC supply loop, significant radiation is generated at that frequency. The noise source from T-CON interferes with the DC supply loop between the DC-to-DC supply converter and the source driver IC. The noise source excites the DC supply loop and generates common- and differential-mode currents in the DC supply loop. Theoretically, much more radiated emission is generated by the common-mode current than from differential-mode current. Therefore, the common-mode current is the dominant source of radiated emission on the PCB driver board of a TFT-LCD panel. Notably, the perimeter of the DC supply loop is very small about a twentieth of wavelength at 140 MHz. Therefore, the DC supply loop is not becoming an efficient radiating loop antenna at 140 MHz, and hence the associated radiation effects are ignored in this study.

In this work, a VNA with a BCI probe was used to measure the common-mode current of the DC supply loop on a PCB. Consistent with Ampere's circuital law, the x -directed currents should induce the magnetic field around x -axis and the y -directed currents should induce the magnetic field around y -axis. Therefore, the BCI probe that is oriented perpendicularly to the x -axis of the Cartesian coordinates can be used to measure the magnetic field that is induced by the x -directed

currents in the DC supply loop on the PCB. By 90° rotation of BCI probe, the BCI probe can be used to measure the magnetic field that is induced by the x -directed and y -directed common-mode currents. Therefore, in accurately measuring the common-mode currents in the DC supply loop on PCB, the orientation of the BCI probe and the DC supply loop on PCB are the most important considerations.

In this case, however, the excitation of common-mode currents on the DC supply loop produces the in-phase x -directed components and out-of-phase y -directed components between the power trace and the ground trace. The x -directed common-mode currents on the DC supply loop are dominant. Therefore, the BCI probe measures only the magnetic field induced by the x -directed common-mode current. Figure 6 reveals that the BCI probe is oriented perpendicularly to the DC supply loop on PCB and it is used only to measure x -directed common-mode currents in the DC supply loop on PCB. Figure 6 also shows the experimental setup for measuring the transmission coefficient needed to characterize the common-mode radiation from the same DC supply loop on PCB as measured earlier by VNA to obtain the input impedance. Figure 6 shows a two-port measurement configuration with a VNA and a BCI probe. One port of the VNA is connected to the DC supply loop on PCB that is inserted into the center hole of the BCI probe. The other port of the VNA is connected to the BCI probe. Figure 6(b) shows the EM simulation corresponding to the experimental setup in Figure 6(a). Figure 7 compares the transmission coefficients of common-mode radiation from the DC supply loop on PCB that were obtained by measurement

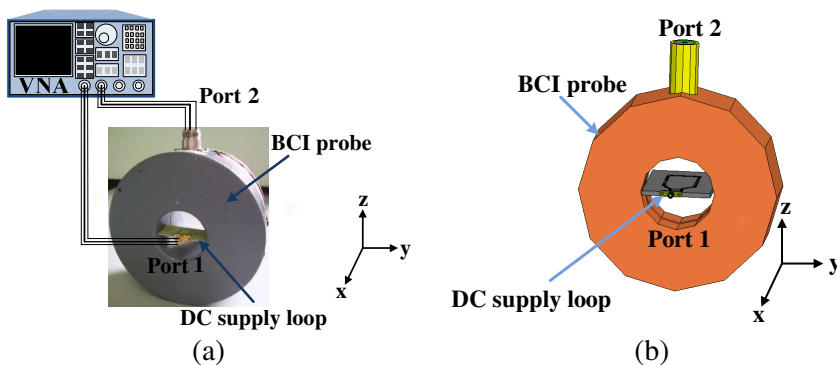


Figure 6. Experimental setup for measuring transmission coefficient of the DC supply loop. (a) Corresponding photograph. (b) Corresponding EM simulation configuration.

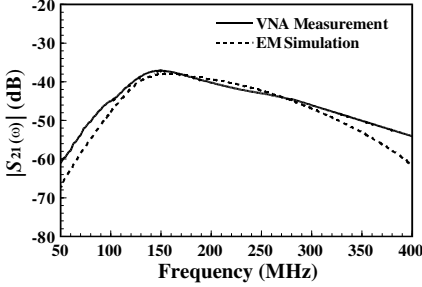


Figure 7. Comparison of transmission coefficient magnitude of the DC supply loop between VNA measurement and EM simulation.

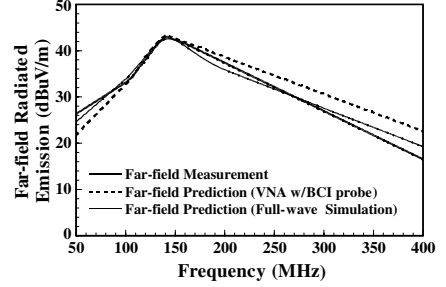


Figure 8. Comparison of far-field radiated emissions from the DC supply loop obtained in fully-anechoic chamber with predictions based on VNA measurement and full-wave simulation.

and EM simulation. All results agreed well in the frequency range 50–400 MHz. Figure 7 indicates that the peak magnitude is at a resonant frequency of 140 MHz, which is consistent with experimental evidence. The data of transmission coefficient $S_{21}(\omega)$ was further used to determine the common-mode current on DC supply loop as follows.

$$I_{CM}(\omega) = |V_{BCI}(\omega)/Z_T(\omega)| = |S_{21}(\omega)V_{inc}/Z_T(\omega)| \quad (9)$$

where $V_{BCI}(\omega)$ is the induced voltage on the BCI probe, V_{inc} the incident voltage to the DC supply loop, and $Z_T(\omega)$ the transfer impedance of the BCI probe. Notably, $V_{BCI}(\omega)$ is the output voltage of port 2, and V_{inc} is in practice estimated from the input power. Notably, $Z_T(\omega)$ is given by (1) obtained from a default process of calibration of the BCI probe.

3.4. Radiation from DC Supply Loop

A Hertzian dipole model demonstrates that the far-field radiated emission because of the measured common-mode current on the DC supply loop is given by [23]

$$E_{C_{max}}(\omega) = 6.28 \times 10^{-7} \frac{I_{CM}(\omega) \cdot L \cdot \omega}{2\pi R} \quad (10)$$

where L is the length of the trace, ω the operating angular frequency, and R the distance between the measurement point and the DC supply loop on PCB.

The far-field measurement of radiated emission from the DC supply loop was performed in a fully-anechoic chamber. A signal

generator provided a 0 dBm input to the DC supply loop with a frequency sweep from 50 to 400 MHz. The DC supply loop was oriented horizontally 1 m above the ground plane of the chamber and 1 m away from the receiving bilog antenna. The power that was received from the antenna was detected using a spectrum analyzer. Figure 8 compares the far-field radiated emissions that were measured in the fully-anechoic chamber with the predictions made using (10) and using the Ansoft HFSS. All results agree closely throughout the measurement frequency range. The radiation was maximal at approximately 140 MHz when the DC supply loop on PCB was at resonance. This phenomenon coincides with earlier observations of the PCB resonance effect.

4. IMPROVEMENT AND ASSESSMENT METHODS

The proposed method was verified by using it to predict the measured spectrum and the predicted spectrum was used to evaluate conformity to EMC regulations. The radiated emission at approximately 140 MHz may be the main radiation mechanisms because DC supply loop may behave like an antenna, radiating the noise source that is coupled from the T-CON. In this study, a very effective and simple method of improving radiated emission is used to reduce radiated emission from a DC supply loop on PCB. The VNA with a BCI probe is also used to predict the reduction of radiated emission. This improvement method involves selecting a reasonable value of the decoupling capacitor of the DC supply loop on PCB. A SMT decoupling capacitor of 22 pF, an ESL of 0.53 nH, and an ESR of 0.077Ω , was implemented. As mentioned in Figure 4, the DC supply loop on the PCB driver board of the TFT-LCD panel was duplicated on another PCB. The input impedance of the DC supply loop was measured using the VNA with an SMA connector. Figures 9(a) and 9(b) compare the real and imaginary parts of the input impedance of the DC supply loop when the improvement method was applied. The solid line represents the measured results made without application of the improvement method and the dotted line represents the measured results made when the improvement method was applied. Additionally, the resonant frequency of the DC supply loop was shifted to 247 MHz when the improvement method was applied. Figure 10 compares the transmission coefficients of common-mode radiation from the DC supply loop on PCB that were obtained by measurement and EM simulation. All results agreed well in the frequency range 50–400 MHz. As can be seen from Figure 10, the magnitude reaches its peak at the resonant frequency of 247 MHz. Clearly the magnitude of the DC supply loop reached its peak at the resonant frequency of

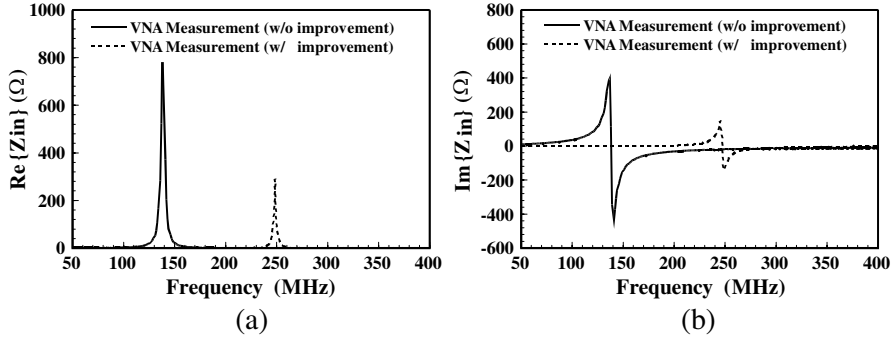


Figure 9. Comparison of measured input impedance of the DC supply loop between with and without improvement method. (a) Input resistances. (b) Input reactances.

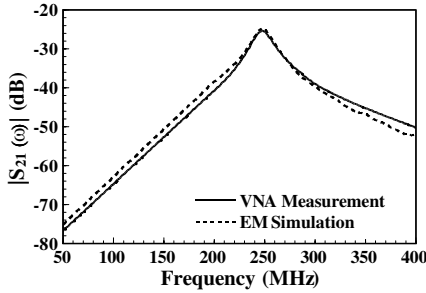


Figure 10. Comparison of transmission coefficient magnitude of the DC supply loop with improvement method between VNA measurement and EM simulation.

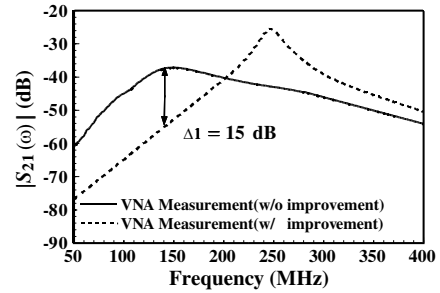


Figure 11. Comparison of measured transmission coefficient magnitude of the DC supply loop between with and without improvement method.

247 MHz, which is consistent with earlier experimental evidence that that resonant frequency was shifted.

Figure 11 presents the improvement ratios of the transmission coefficient (S_{21}). The solid line represents the measured results made without applying the improvement method and the dotted line represents the measured results made when the improvement method was used to reduce the radiated emission. The improvement ratio of the transmission coefficient (S_{21}) at approximately 140 MHz is approximately 15 dB in the range of frequencies over which the measured results were made. According to empirical experience, the far-field radiated emission DC supply loop was also significantly

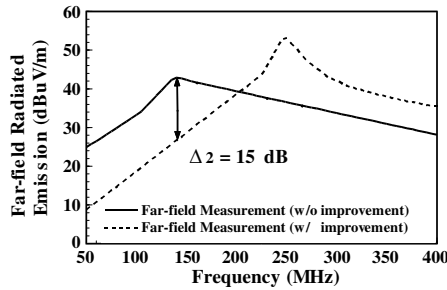


Figure 12. Comparison of measured far-field radiated emission magnitude from a DC supply loop between with and without improvement method.

reduced. From the improvement ratio of the common-mode current, which is clearly shown in Figure 12, the radiated emission from the DC supply loop decreased by an improvement of 15 dB in same range of frequencies. The selecting a reasonable value of the decoupling capacitor causes a dramatic reduction in the far-field radiated emissions.

In Summary, the common-mode current and far-field measured results demonstrate that improvement method was applied, and the resonant frequency of the DC supply loop on PCB was shifted to 247 MHz. Restated, the improvement method can be used to shift the resonant frequencies of a DC supply loop on PCB. The measured radiated emissions correlate well with the predictions made using the transmission coefficient. Clearly the agreement in Figure 12 inspires confidence in the ability of the proposed method of common-mode current measurement using VNA and a BCI probe to predict the radiated emission from a DC supply loop on PCB. Compared to existing common-mode current and far-field measurements, the proposed method has the advantages of saving cost, time and space in determining the common-mode radiation properties of a PCB.

5. CONCLUSION

This work proposed a method for measuring the transmission coefficient to characterize the common-mode radiation from PCB using a VNA with a BCI probe. The far-field radiated emissions obtained from such measured results can be used to confirm compliance with EMC regulations. The proposed method was demonstrated using an example of common-mode radiation from a DC supply on

PCB. The far-field radiated emissions from the DC supply on PCB that was determined from VNA measurement, fully-anechoic chamber measurement, and electromagnetic simulation agreed closely with each other. With assistance of a VNA with a BCI probe, the radiated emission from a DC supply on PCB can be evaluated effectively. The VNA with a BCI probe can be further used to determine the reduction of radiated emission from a DC supply loop. The far-field radiated emissions from the a DC supply on PCB were thus reduced by an average of 15 dB. The predictions agree closely with the relevant measured results.

REFERENCES

1. Luo, M. and K.-M. Huang, "An extended delay-rational macromodel for electromagnetic interference analysis of mixed signal circuits," *Progress In Electromagnetics Research*, Vol. 127, 189–210, 2012.
2. Ding, T.-H., Y.-S. Li, X. Yan, and Y.-Z. Qu, "A new efficient method for calculation and suppression of simultaneous switching noise with the time-domain impedance function for high-speed circuit design," *Progress In Electromagnetics Research*, Vol. 112, 41–62, 2011.
3. Wu, B. and H. L. Lo, "Methods and designs for improving the signal integrity of vertical interconnects in high performance packaging," *Progress In Electromagnetics Research*, Vol. 123, 1–11, 2012.
4. Horng, T. S. and S. M. Wu, "Radiation from a microstrip amplifier," *IEEE Trans. on Microwave Theory and Tech.*, Vol. 5, 2005–2010, Aug. 2002.
5. Kwon, J. H. and H. D. Choi, "Experimental verification of correlation algorithm between FAC and open area test site/SAC," *IEEE Int. Symp. Electromagn. Compat.*, 910–914, Aug. 2003.
6. Li, P. and L. Jiang, "The far field transformation for the antenna modeling based on spherical electric field measurements," *Progress In Electromagnetics Research*, Vol. 123, 243–261, 2012.
7. Chen, X., "Measurements and evaluations of multi-element antennas based on limited channel samples in a reverberation chamber," *Progress In Electromagnetics Research*, Vol. 131, 45–62, 2012.
8. Staniec, K., "Evaluation of the ZigBee transmission repetition mechanism in the variably-loaded reverberation chamber," *Progress In Electromagnetics Research*, Vol. 132, 297–314, 2012.

9. Yan, W., J.-D. Xu, N.-J. Li, and W. Tan, "A novel fast near-field electromagnetic imaging method for full rotation problem," *Progress In Electromagnetics Research*, Vol. 120, 387–401, 2011.
10. Qureshi, M. A., C. H. Schmidt, and T. F. Eibert, "Adaptive sampling in multilevel plane wave based near-field far-field transformed planar near-field measurements," *Progress In Electromagnetics Research*, Vol. 126, 481–497, 2012.
11. Lotito, V., U. Sennhauser, C. V. Hafner, and G.-L. Bona, "Interaction of an asymmetric scanning near field optical microscopy probe with fluorescent molecules," *Progress In Electromagnetics Research*, Vol. 121, 281–299, 2011.
12. Liao, C.-C. and Y.-L. Lo, "Phenomenological model combining dipole-interaction signal and background effects for analyzing modulated detection in apertureless scanning near-field optical microscopy," *Progress In Electromagnetics Research*, Vol. 112, 415–440, 2011.
13. Chevallier, D., D. Baudry, and A. Louis, "Improvement of electrical near-field measurements with an electro-optic test bench," *Progress In Electromagnetics Research B*, Vol. 40, 381–398, 2012.
14. Chen, K. S., T. S. Horng, C. Y. Ho, J. M. Wu, and K. C. Peng, "Diagnosis of EMI to laptop WWAN device from TFT-LCD driver using non-contact measurement-based transfer function technique," *IEEE Int. Symp. Electromagn. Compat.*, 301–304, Jul. 2010.
15. Bockelman, D. E. and W. R. Eisenstadt, "Combined differential and common-mode scattering parameters — Theory and simulation," *IEEE Trans. on Microwave Theory and Tech.*, Vol. 43, 1530–1539, Jul. 1995.
16. Chen, C., "Examination of electronic module immunity using transfer functions," *IEEE Int. Symp. Electromagn. Compat.*, 756–761, Aug. 2005.
17. Grassi, F., F. Marliani, and S. A. Pignari, "Circuit modeling of injection probes for bulk current injection," *IEEE Trans. on Electromagn. Compat.*, Vol. 49, No. 3, 563–576, Aug. 2007.
18. Ho, C.-Y., K.-S. Chen, and T.-S. Horng, "Prediction of common-mode radiated emission from PCB using vector network analyzer with a bulk injection current probe," *Journal of Electromagnetic Waves and Applications*, Vol. 26, No. 16, 2121–2129, 2012.
19. Choi, S. P., J. W. Kwon, K. E. Chang, J. T. Kim, and M. K. Han, "EMI analysis of TFT-LCD driver IC," *Proc. 17th Int. Zurich Symp. Electromagn. Compat.*, 606–609, 2006.

20. Han, S. M., J.-J. Bang, C.-S. Huh, and J.-S. Choi, "A PCB noise analysis regarding emp penetration using an electromagnetic topology method," *Progress In Electromagnetics Research*, Vol. 122, 15–27, 2012.
21. Li, Z., L. L. Liu, and C. Q. Gu, "Generalized equivalent cable bundle method for modeling emc issues of complex cable bundle terminated in arbitrary loads," *Progress In Electromagnetics Research*, Vol. 123, 13–30, 2012.
22. Eudes, T., B. Ravelo, and A. Louis, "Transient response characterization of the high-speed interconnection rlcg-model for the signal integrity analysis," *Progress In Electromagnetics Research*, Vol. 112, 183–197, 2011.
23. Paul, C. R., "A comparison of the contributions of common-mode and differential-mode currents in radiated emissions," *IEEE Trans. on Electromagn. Compat.*, Vol. 31, No. 2, 189–193, May 1989.